



Contents lists available at ScienceDirect

## Journal of the Mechanics and Physics of Solids

journal homepage: [www.elsevier.com/locate/jmps](http://www.elsevier.com/locate/jmps)

# Torsion and bending periodic boundary conditions for modeling the intrinsic strength of nanowires

Wei Cai \*, William Fong, Erich Elsen, Christopher R. Weinberger

Department of Mechanical Engineering, Stanford University, CA 94305-4040, USA

## ARTICLE INFO

### Article history:

Received 10 March 2008  
Received in revised form  
3 June 2008  
Accepted 11 July 2008

### Keywords:

Elastic properties  
Microstructure  
Fracture  
Numerical algorithms

## ABSTRACT

We present a unified approach for atomistic modeling of torsion and bending of nanowires that is free from artificial end effects. Torsional and bending periodic boundary conditions (t-PBC and b-PBC) are formulated by generalizing the conventional periodic boundary conditions (PBC) to cylindrical coordinates. The approach is simpler than the more general objective molecular dynamics formulation because we focus on the special cases of torsion and bending. A simple implementation of these boundary conditions is presented and correctly conserves linear and angular momenta. We also derive the virial expressions for the average torque and bending moment under these boundary conditions that are analogous to the virial expression for the average stress in PBC. The method is demonstrated by molecular dynamics simulation of Si nanowires under torsion and bending, which exhibit several modes of failure depending on their diameters.

© 2008 Elsevier Ltd. All rights reserved.

## 1. Introduction

Recently there has been considerable interest in the directed growth of semiconductor nanowires (NWs), which can be used to construct nanoscale field effect transistors (FETs) (Cui et al., 2003; Wang et al., 2003; Huang and Lieber, 2004), chemical and biological sensors (Cui et al., 2001), nanoactuators (Chau et al., 2003) and nanofluidic components (Fan et al., 2005). Epitaxially grown NWs have the potential to function as conducting elements between different layers of three-dimensional integrated circuits. Because significant stress may build up during fabrication and service (e.g. due to thermal or lattice mismatch), characterization and prediction of mechanical strength and stability of NWs is important for the reliability of these novel devices.

NWs also offer unique opportunities for studying the fundamental deformation mechanisms of materials at the nanoscale. The growing ability to fabricate and mechanically test microscale and nanoscale specimens and the increasing computational power allows for direct comparison between experiments and theory at the same length scale.

The size of these devices presents a challenge to test their mechanical properties. In macroscale samples, the materials are routinely tested in tension, shear, torsion and bending using standard grips and supports. Smaller samples, however, require more inventive testing techniques. For nanoscale testing, tensile and bending tests have been performed using nanoindentors, AFM (Kizuka et al., 2005; Ding et al., 2006), and MEMS devices (Zhu and Espinosa, 2005; Isono et al., 2006). Similar experiments have been performed at the microscale (Jeff and Fleck, 1994; Stölken and Evans, 1998). With the rapid

\* Corresponding author. Tel.: +1408 892 7611.

E-mail addresses: [caiwei@stanford.edu](mailto:caiwei@stanford.edu) (W. Cai), [willfong@stanford.edu](mailto:willfong@stanford.edu) (W. Fong), [eelsen@stanford.edu](mailto:eelsen@stanford.edu) (E. Elsen), [cweinber@stanford.edu](mailto:cweinber@stanford.edu) (C.R. Weinberger).

progress of nanofabrication and nanomanipulation capabilities, additional tension, torsion, and bending experimental data on crystalline and amorphous NWs will soon be available.

Molecular dynamics is poised to be the main theoretical tool to help understand and predict small scale mechanical properties. However, since MD is limited in the number of atoms it can simulate; it cannot simulate whole NWs. Either the NW simulated must be extremely short or periodic boundary conditions (PBC) must be used. End conditions artificially alter the material locally such that defect nucleation and failure often occurs there. This results in simulations that test the strength of the boundary rather than the intrinsic strength of the material. Traditional PBC remove this artifact by enforcing translational invariance and eliminating all artificial boundaries.

The use of conventional PBC allows for the simulation of tensile, pure shear, and simple shear in MD (Parrinello and Rahman, 1981). In fact, the mechanical properties of silicon NWs in tension were recently calculated using this approach (Kang and Cai, 2007). The NWs were strained by extending the periodicity along the NW length and the stress was calculated through the virial formula. However, regardless of the types of strain imposed on the periodic simulation cell, the images form a perfect lattice which precludes non-zero average torsion or bending. Therefore, to simulate torsion or bending tests, either small finite NWs must be simulated or the current PBC framework must be altered.

Many molecular dynamics simulations on torsion and bending of nanoscale structures have been reported (Horstemeyer et al., 2002; Zhang and Shen, 2006; Nozaki et al., 2002; Huhtala et al., 2004; Mylvaganam et al., 2006). The artificial end effects are sometimes reduced by putting the ends far away from the region undergoing severe deformation, requiring a long NW (Makeev and Srivastava, 2006). There have also been attempts to rectify this problem (Nakatani and Kitagawa, 2004). Recently, the objective molecular dynamics (OMD) formulation (Dumitrica and James, 2007) has been proposed that generalizes PBC to accommodate symmetries other than translational. Under this framework, torsion and bending simulations can be performed without end effects. But the general formulation of OMD is somewhat difficult to apply to existing MD simulation programs.

In this paper, we present a simpler formulation that accommodates torsion and bending in a generalized PBC framework. From this simple formulation we found that torsion and bending can be related to shear and normal strains when expressed in *cylindrical coordinates*. This leads to t-PBC and b-PBC, respectively, as formulated in Section 2. While only linear momenta are preserved in PBC, both t-PBC and b-PBC preserve the angular momentum around their rotation axes. These new boundary conditions can be easily implemented on top of existing simulation programs that use conventional PBC. In Section 3, we derive the virial expressions for the torque and bending moment that are analogous to the virial expressions for the average stress in simulation cells under PBC. The virial expressions of torque and bending moment, expressed as a sum over discrete atoms, are found to correspond to a set of tensorial quantities in continuum mechanics, expressed as a volume integral. Section 4 presents the application of these new boundary conditions to modeling of the intrinsic strength of Si NWs under torsion and bending.

## 2. Generalization of PBC

### 2.1. Review of conventional PBC

PBC can be visualized as a primary cell surrounded by a set of replicas, or image cells. The replicas are arranged into a regular lattice specified by three repeat vectors:  $\mathbf{c}_1$ ,  $\mathbf{c}_2$ ,  $\mathbf{c}_3$ . This means that whenever there is an atom at location  $\mathbf{r}_i$ , there are also atoms at  $\mathbf{r}_i + n_1\mathbf{c}_1 + n_2\mathbf{c}_2 + n_3\mathbf{c}_3$ , where  $n_1, n_2, n_3$  are arbitrary integers (Allen and Tildesley, 2007; Bulatov and Cai, 2006). Because the atoms in the image cells behave identically as those in the primary cell, it is immaterial to specify which space belongs to the primary cell and which space belongs to the image cell. Even though it is customary to refer to the parallelepiped formed by the three period vectors as the simulation cell and the surface of this parallelepiped as the boundary, there is no physical interface at this boundary. In other words, the “boundary” between the primary and image cells in PBC can be drawn anywhere and is only a matter of convention. Consequently, translational invariance is preserved and linear momenta is conserved in all three directions. It is customary to set the velocity of the center of mass to zero in the initial condition which should remain zero during the simulation. This provides an important check of the self-consistency of the simulation program.

The scaled coordinates  $\mathbf{s}_i$  are usually introduced to simplify the notation and the implementation of PBC, where

$$\mathbf{r}_i = \mathbf{H} \cdot \mathbf{s}_i \quad (1)$$

and  $\mathbf{H} = [\mathbf{c}_1|\mathbf{c}_2|\mathbf{c}_3]$  is a  $3 \times 3$  matrix whose three columns are formed by the coordinates of the three repeat vectors. For example,  $\mathbf{H}$  becomes a diagonal matrix when the three repeat vectors are parallel to the  $x$ -,  $y$ -,  $z$ -axes, respectively,

$$\mathbf{H} = \begin{bmatrix} L_x & 0 & 0 \\ 0 & L_y & 0 \\ 0 & 0 & L_z \end{bmatrix} \quad (2)$$

where  $L_x = |\mathbf{c}_1|$ ,  $L_y = |\mathbf{c}_2|$ ,  $L_z = |\mathbf{c}_3|$ . The PBC can also be stated in terms of the scaled coordinates as follows: whenever there is an atom at location  $\mathbf{s}_i = (s_x^i, s_y^i, s_z^i)^T$ , there are also atoms at location  $(s_x^i + n_1, s_y^i + n_2, s_z^i + n_3)^T$ , where  $n_1, n_2, n_3$  are arbitrary integers. The scaled coordinates of each atom,  $s_x^i, s_y^i, s_z^i$  are sometimes limited to  $[-0.5, 0.5)$ , although this is not necessary.

To apply a normal strain in the  $x$ -direction, we only need to modify the magnitude of  $L_x$ . To introduce a shear strain  $\varepsilon_{yz}$ , we can simply add an off-diagonal term to the  $\mathbf{H}$  matrix:

$$\mathbf{H} = \begin{bmatrix} L_x & 0 & 0 \\ 0 & L_y & 2\varepsilon_{yz}L_z \\ 0 & 0 & L_z \end{bmatrix} \quad (3)$$

Regardless of the normal or shear strain, the scaled coordinates,  $s_x^i, s_y^i, s_z^i$ , still independently satisfy PBC in the domain  $[-0.5, 0.5]$ , which is the main advantage for introducing the scaled coordinates. By modifying  $\mathbf{H}$  in these ways, we can stretch and shear a crystal in MD.

## 2.2. Torsional PBC

While the exact formulation of PBC as stated above cannot accommodate a non-zero average torsion over the entire simulation cell, the general idea can still be used. Consider an NW of length  $L_z$  aligned along the  $z$ -axis, as shown in Fig. 1(a). To apply PBC along the  $z$ -axis, we can make two copies of the atoms in the NW, shift them along  $z$  by  $\pm L_z$ , and let them interact with the atoms in the primary wire. Two copies of the original NW would be sufficient if the cut-off radius  $r_c$  of the interatomic potential function is smaller than  $L_z$  (usually  $r_c \ll L_z$ ). After PBC is applied, the model may be considered as an infinitely long, periodic wire along the  $z$ -axis. Any arbitrary section of length  $L_z$  can now be considered as the primary wire due to the periodicity. Since the atomic arrangement must repeat itself after every  $L_z$  distance along the wire, the average torsion we can apply to the NW is zero. A local torsion in some section of the wire has to be canceled by an opposite torsion at another section that is less than  $L_z$  away.

One way to introduce an average torque to this infinitely long wire is to rotate the two images by angle  $+\phi$  and  $-\phi$ , respectively, before we attach them to the two ends of the primary wire as shown in Fig. 1(b). The image wire that is displaced by  $L_z$  is rotated by  $\phi$ , while the one that is displaced by  $-L_z$  is rotated by  $-\phi$ . In this case, as we travel along the wire by  $L_z$ , we will find that the atomic arrangement in the cross-section will be rotated around  $z$ -axis by angle  $\phi$  but otherwise identical. Again, because this property is satisfied by any cross-section of the NW, it is arbitrary which we call the primary wire and which we call images similar to conventional PBC. The torsion imposed on the NW can be characterized by the angle of rotation per unit length,  $\phi/L_z$ . In the limit of small deformation, the shear strain field produced by the torsion is

$$\varepsilon_{\theta z} = \frac{r\phi}{2L_z} \quad (4)$$

where  $r$  is the distance away from the  $z$ -axis.

The above procedure specifies torsional periodic boundary conditions (t-PBC) that can be easily expressed in terms of scaled cylindrical coordinates. Consider an atom  $i$  with cartesian coordinates  $\mathbf{r}_i = (x_i, y_i, z_i)^T$  and cylindrical coordinates  $(r_i, \theta_i, z_i)^T$ , which are related to each other by

$$x_i = r_i \cos \theta_i \quad (5)$$

$$y_i = r_i \sin \theta_i \quad (6)$$

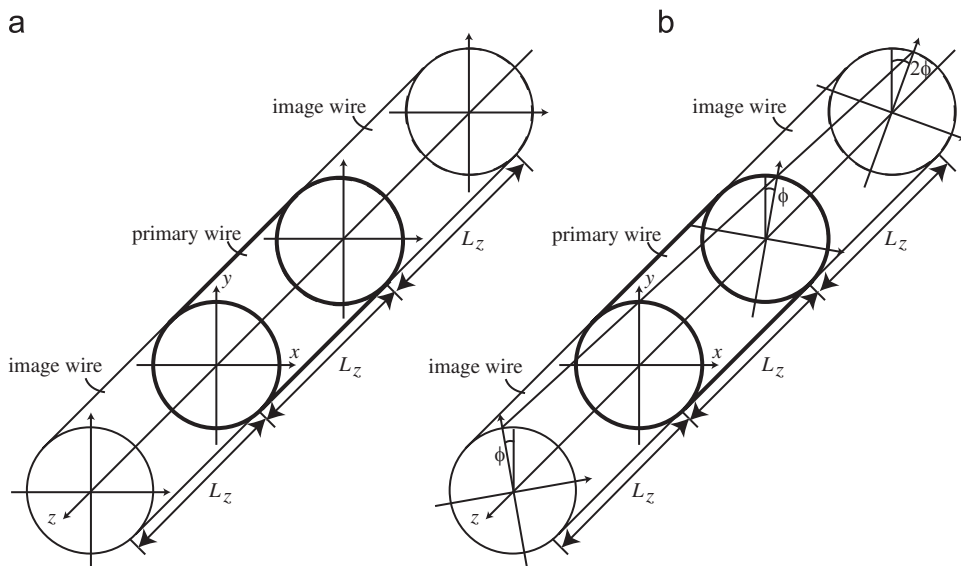


Fig. 1. (a) A nanowire subjected to PBC along  $z$ -axis. (b) A nanowire subjected to t-PBC along  $z$ -axis.

When the wire is subjected to PBC along  $z$  (with free boundary conditions in  $x$  and  $y$ ), we introduce the scaled cylindrical coordinates  $(s_r^i, s_\theta^i, s_z^i)^T$  through the relationship

$$\begin{pmatrix} r_i \\ \theta_i \\ z_i \end{pmatrix} = \begin{bmatrix} R & 0 & 0 \\ 0 & 2\pi & 0 \\ 0 & 0 & L_z \end{bmatrix} \begin{pmatrix} s_r^i \\ s_\theta^i \\ s_z^i \end{pmatrix} \equiv \mathbf{M} \begin{pmatrix} s_r^i \\ s_\theta^i \\ s_z^i \end{pmatrix} \quad (7)$$

Both  $s_\theta^i$  and  $s_z^i$  independently satisfy PBC in the domain  $[-0.5, 0.5)$ . No boundary condition is applied to coordinate  $s_r^i$ .  $R$  is a characteristic length scale in the radial direction in order to make  $s_r^i$  dimensionless. Although this is not necessary, one can choose  $R$  to be the radius of the NW, in which case  $s_r^i$  would vary from 0 to 1.

Torsion can be easily imposed by introducing an off-diagonal term to the matrix  $\mathbf{M}$ , which becomes

$$\mathbf{M} = \begin{bmatrix} R & 0 & 0 \\ 0 & 2\pi & \phi \\ 0 & 0 & L_z \end{bmatrix} \quad (8)$$

The scaled coordinates,  $s_\theta^i$  and  $s_z^i$ , still independently satisfy PBC in the domain  $[-0.5, 0.5)$ . This is analogous to the application of shear strain to a simulation cell subjected to conventional PBC, as described in Eq. (3). t-PBC can be easily implemented in an existing simulation program by literally following Fig. 1(b), i.e. by making two copies of the wire, rotating them by  $\pm\phi$ , and placing the two copies at the two ends of the primary wire. In practice, it is not necessary to copy the entire wire, because the cut-off radius  $r_c$  of the interatomic potential function is usually much smaller than  $L_z$ . Only two sections at the ends of the primary wire with lengths longer than  $r_c$  need to be copied.<sup>1</sup> It is important to perform this operation of “copy-and-paste” at every MD time step, or whenever the potential energy and atomic forces need to be evaluated. This will completely remove the end effects and will ensure that identical MD trajectories will be generated had we chosen a different section (also of length  $L_z$ ) of the wire as our primary wire.

An important property of the t-PBC is that the trajectory of every atom satisfy the classical (Newton’s) equation of motion. In other words, among the infinite number of atoms that are periodic images of each other, it makes no physical difference as to which one should be called “primary” and which ones should be called “images”. Since the primary atoms follow Newton’s equation of motion ( $\mathbf{f}_i = m\mathbf{a}_i$ ), to prove the above claim it suffices to show that the image atoms, which are slaves of the primary atoms (through the “copy-and-paste” operation) also follow Newton’s equation of motion ( $\mathbf{f}_i = m\mathbf{a}_i$ ).

To show this, consider an atom  $i$  and its periodic image  $i'$ , such that  $s_r^{i'} = s_r^i$ ,  $s_\theta^{i'} = s_\theta^i$ ,  $s_z^{i'} = s_z^i + 1$ . The position of the two atoms are related by t-PBC:  $\mathbf{r}_{i'} = \text{Rot}_z(\mathbf{r}_i, \phi) + \hat{\mathbf{e}}_z L_z$ , where  $\text{Rot}_z(\cdot, \phi)$  represent rotation of a vector around  $z$ -axis by angle  $\phi$  and  $\hat{\mathbf{e}}_z$  is the unit vector along  $z$ -axis. Hence the acceleration of the two atoms are related to each other through:  $\mathbf{a}_{i'} = \text{Rot}_z(\mathbf{a}_i, \phi)$ . Now consider an arbitrary atom  $j$  that falls within the cut-off radius of atom  $i$ . Let  $\mathbf{r}_{ij} \equiv \mathbf{r}_j - \mathbf{r}_i$  be the distance vector from atom  $i$  to  $j$ . Consider the image atom  $j'$  such that  $s_r^{j'} = s_r^j$ ,  $s_\theta^{j'} = s_\theta^j$ ,  $s_z^{j'} = s_z^j + 1$ . Hence  $\mathbf{r}_{ij'} = \text{Rot}_z(\mathbf{r}_{ij}, \phi) + \hat{\mathbf{e}}_z L_z$ , and  $\mathbf{r}_{ij'} \equiv \mathbf{r}_{j'} - \mathbf{r}_{i'} = \text{Rot}_z(\mathbf{r}_{ij}, \phi)$ . Since this is true for an arbitrary neighbor atom  $j$  around atom  $i$ , the forces on atoms  $i$  and  $i'$  must satisfy the relation:  $\mathbf{f}_{i'} = \text{Rot}_z(\mathbf{f}_i, \phi)$ . Therefore, the trajectory of atom  $i'$  also satisfies Newton’s equation of motion  $\mathbf{f}_{i'} = m\mathbf{a}_{i'}$ .

MD simulations under t-PBC should conserve the total linear momentum  $P_z$  and angular momentum  $J_z$  because t-PBC preserves both translational invariance along and rotational invariance around the  $z$ -axis. However, the linear momenta  $P_x$  and  $P_y$  are no longer conserved in t-PBC due to the specific choice of the origin in the  $x$ - $y$  plane (which defines the cylindrical coordinates  $r$  and  $\theta$ ). In comparison, the angular momentum  $J_z$  is usually not conserved in PBC. Consequently, at the beginning of MD simulations under t-PBC, we need to set both  $P_z$  and  $J_z$  to zero.  $P_z$  and  $J_z$  will remain zero, which provides an important self-consistency check of the implementation of boundary conditions and numerical integrators.

### 2.3. Bending PBC

The same idea can be used to impose bending deformation on wires. Again, we will describe the atomic positions through scaled cylindrical coordinates,  $(s_r^i, s_\theta^i, s_z^i)^T$ , which is related to the real cylindrical coordinates,  $(r^i, \theta^i, z^i)^T$ , through the following transformation:

$$\begin{pmatrix} r_i \\ \theta_i \\ z_i \end{pmatrix} = \begin{bmatrix} R & 0 & 0 \\ 0 & \Theta & 0 \\ 0 & 0 & L_z \end{bmatrix} \begin{pmatrix} s_r^i \\ s_\theta^i \\ s_z^i \end{pmatrix} + \begin{pmatrix} L_0/\Theta \\ 0 \\ 0 \end{pmatrix} \equiv \mathbf{N} \begin{pmatrix} s_r^i \\ s_\theta^i \\ s_z^i \end{pmatrix} + \begin{pmatrix} L_0/\Theta \\ 0 \\ 0 \end{pmatrix} \quad (9)$$

While the coordinate system here is still the same as that in the case of torsion, the wire is oriented along the  $\theta$ -direction, as shown in Fig. 2. Among the three scaled coordinates, only  $s_\theta^i$  is subjected to a PBC, in the domain of  $[-0.5, 0.5)$ . This means that  $\theta^i$  is periodic in the domain  $[-\Theta/2, \Theta/2)$ . No boundary conditions are applied to  $s_r^i$  and  $s_z^i$ .  $R$  and  $L_z$  are characteristic length scales in the  $r$ - and  $z$ -directions, respectively.  $L_0$  is the original

<sup>1</sup> This simple approach is not able to accommodate long-range Coulomb interactions, for which the Ewald summation is usually used in conventional PBC. Extension of the Ewald method to t-PBC is beyond the scope of this paper.

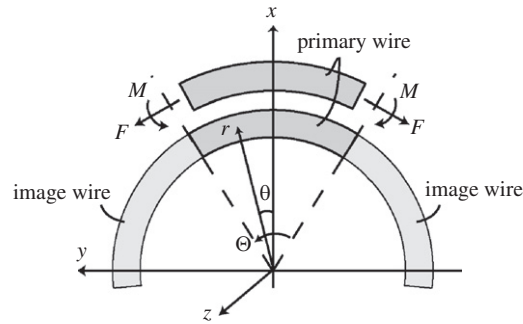


**Fig. 2.** A nanowire subjected to b-PBC around  $z$ -axis. At equilibrium the net line tension force  $F$  must vanish but a non-zero bending moment  $M$  will remain.

(stress free) length of the wire and  $\rho = L_0/\Theta$  is the radius of curvature of the wire. The equation  $r = \rho$  specifies the neutral surface of the wire. Thus,  $r_i = \rho + Rs_r^i$ , where  $Rs_r^i$  describes the displacement of atom  $i$  away from the neutral axis in the  $r$ -direction.

In the previous section, an off-diagonal element has to be introduced to the transformation matrix  $\mathbf{M}$  in order to introduce torsion. In comparison, the form of Eq. (9) does not need to be changed to accommodate bending. Different amount of bending can be imposed by adjusting the value  $\Theta$ , while the matrix  $\mathbf{N}$  remains diagonal. The larger  $\Theta$  is the more severe the bending deformation. The state of zero bending corresponds to the limit of  $\Theta \rightarrow 0$ .

Intuitively, it may seem that increasing the value of  $\Theta$  would elongate the wire and hence induce a net tension force  $F$  in addition to a bending moment  $M$ . However, this is not the case because the direction of force  $F$  at the two ends of the wire are not parallel to each other, as shown in Fig. 2. When no lateral force (i.e. in the  $r$ -direction) is applied to the wire,  $F$  must vanish for the entire wire to reach equilibrium. Otherwise, there will be a non-zero net force in the  $-x$ -direction, which will cause the wire to move until  $F$  become zero. At equilibrium, only a bending moment (but no tension force) can be imposed by b-PBC.

b-PBC can be implemented in a similar way as t-PBC. We make two copies of the primary wire and rotate them around the  $z$ -axis by  $\pm\Theta$ . The atoms in these copies will interact and provide boundary conditions for atoms in the primary wire.<sup>2</sup> Again, this “copy-and-paste” operation is required at every step of MD simulation. This will ensure all atoms (primary and images) satisfy Newton’s equation of motion. The proof is similar to that given in the previous section for t-PBC and is omitted here for brevity. Interestingly, both the linear momentum  $P_z$  and the angular momentum  $J_z$  for the center of mass are conserved in b-PBC, exactly the same as t-PBC. Therefore, both  $P_z$  and  $J_z$  must be set to zero in the initial condition of MD simulations.

### 3. Virial expressions for torque and bending moment

The experimental data on tensile tests are usually presented in the form of stress–strain curves. The normal stress is calculated from  $\sigma = F/A$ , where  $F$  is the force applied to the ends and  $A$  is the cross-section area of the wire. In experiments on macroscopic samples, the end effects are reduced by making the ends of the specimen much thicker than the middle (gauge) section where significant deformation is expected. In atomistic simulations, on the other hand, the end effects are removed by a different approach, usually through the use of PBC. Unfortunately, with the end effects completely removed by PBC, there is no place to serve as grips where external forces can be applied. Therefore, the stress must be computed differently in atomistic simulations under PBC than in experiments. The virial stress expression is widely used in atomistic calculations, which represents the time and volume average of stress in the simulation cell.

The same problem appears in atomistic simulations under t-PBC and b-PBC. There needs to be a procedure to compute the torque and bending moment in these new boundary conditions. In this section, we develop virial expressions for the torque and bending moment in t-PBC and b-PBC. Similar to the virial stress, the new expressions involve discrete sums over all atoms in the simulation cell. The corresponding expressions in continuum mechanics, expressed in terms of volume integrals, are also identified. Since the derivation of these new expressions are motivated by that of the original virial expression, we will start with a quick review of the virial stress.

<sup>2</sup> Similar to the case of t-PBC, this simple approach is not able to accommodate long-range Coulomb interactions. While a wire under t-PBC can be visualized as an infinitely long wire, this interpretation will encounter some difficulty in b-PBC, because continuing the curved wire along the  $\theta$ -direction will eventually make the wire overlap. The interpretation of b-PBC would then require the wire to exist in a multi-sheeted Riemann space (Sommerfeld, 1964, p. 80) so that the wire does not really overlap with each other.

### 3.1. Virial stress in PBC

For an atomistic simulation cell subjected to PBC in all three directions, the virial formula gives the stress averaged over the entire simulation cell at thermal equilibrium as

$$\sigma_{\alpha\beta} = \frac{1}{\Omega} \left\langle \sum_{i=1}^N -m_i v_{\alpha}^i v_{\beta}^i + \sum_{i=1}^{N-1} \sum_{j=i+1}^N \frac{\partial V}{\partial (x_{\alpha}^i - x_{\alpha}^j)} (x_{\beta}^i - x_{\beta}^j) \right\rangle \quad (10)$$

In this formula  $\Omega = \det(\mathbf{H})$  is the volume of the simulation cell,  $N$  is the total number of atoms,  $v_{\alpha}^i$  and  $x_{\alpha}^i$  are the  $\alpha$ -components of the velocity and position of atom  $i$  and  $V$  is the potential energy. The terms  $(x_{\alpha}^i - x_{\alpha}^j)$  and  $(x_{\beta}^i - x_{\beta}^j)$  in the second summation are assumed to be taken from the nearest images of atom  $i$  and atom  $j$ . The bracket  $\langle \cdot \rangle$  means ensemble average, which equals to the long time average if the system has reached equilibrium. Thus the virial stress is the stress both averaged over the entire space and over a long time.

The virial stress is the derivative of the free energy  $F$  of the atomistic simulation cell with respect to a virtual strain  $\varepsilon_{\alpha\beta}$ , which deforms the periodic vectors  $\mathbf{c}_1$ ,  $\mathbf{c}_2$  and  $\mathbf{c}_3$  and hence the matrix  $\mathbf{H}$ :

$$\sigma_{\alpha\beta} = \frac{1}{\Omega} \frac{\partial F}{\partial \varepsilon_{\alpha\beta}} \quad (11)$$

Assuming the simulation cell is in equilibrium under the canonical ensemble, the free energy is defined as

$$F \equiv -k_B T \ln \left\{ \frac{1}{h^{3N} N!} \int d^{3N} \mathbf{r}_i d^{3N} \mathbf{p}_i \exp \left[ -\frac{1}{k_B T} \left( \sum_{i=1}^N \frac{|\mathbf{p}_i|^2}{2m_i} + V(\{\mathbf{r}_i\}) \right) \right] \right\} \quad (12)$$

where  $k_B$  is Boltzmann's constant,  $T$  is temperature,  $h$  is Planck's constant,  $\mathbf{r}_i$  and  $\mathbf{p}_i$  are atomic position and momentum vectors and  $V$  is the interatomic potential function. The momenta can be integrated out explicitly to give

$$F = -k_B T \ln \left\{ \frac{1}{\Lambda^{3N} N!} \int d^{3N} \mathbf{r}_i \exp \left[ -\frac{V(\{\mathbf{r}_i\})}{k_B T} \right] \right\} \quad (13)$$

where  $\Lambda \equiv h/(2\pi m k_B T)^{1/2}$  is the thermal de Broglie wavelength. In atomistic simulations under PBC, the potential energy can be written as a function of the scaled coordinates  $\{\mathbf{s}_i\}$  and matrix  $\mathbf{H}$ . Hence,  $F$  can also be written in terms of an integral over the scaled coordinates:

$$F = -k_B T \ln \left\{ \frac{\Omega^N}{\Lambda^{3N} N!} \int d^{3N} \mathbf{s}_i \exp \left[ -\frac{V(\{\mathbf{s}_i\}, \mathbf{H})}{k_B T} \right] \right\} \quad (14)$$

The virial formula can be obtained by taking the derivative of Eq. (14) with respect to  $\varepsilon_{\alpha\beta}$ . The first term in the virial formula comes from the derivative of the volume  $\Omega$  with respect to  $\varepsilon_{\alpha\beta}$ , which contributes a  $-N k_B T \delta_{\alpha\beta} / \Omega$  term to the total stress. This is equivalent to the velocity term in the virial formula because  $\langle m_i v_{\alpha}^i v_{\beta}^i \rangle = k_B T \delta_{\alpha\beta}$  in the canonical ensemble. The second term comes from the derivative of the potential energy  $V(\{\mathbf{s}_i\}, \mathbf{H})$  with respect to  $\varepsilon_{\alpha\beta}$ . The virial stress expression can also be derived in several alternative approaches (see Tsai, 1979; Marc and McMillian, 1985; Chueng and Yip, 1991; Cormier et al., 2001; Zimmerman et al., 2004 for more discussions). The corresponding quantity for virial stress in continuum mechanics is the volume average of the stress tensor:

$$\bar{\sigma}_{ij} = \frac{1}{\Omega} \int_{\Omega} \sigma_{ij} dV = \frac{1}{\Omega} \oint_S t_j x_i dS \quad (15)$$

where the integral  $\oint_S$  is over the bounding surface of volume  $\Omega$ ,  $t_j$  is the traction force density on surface element  $dS$ , and  $x_i$  is the position vector of the surface element.

### 3.2. Virial torque in t-PBC

The virial torque expression for a simulation cell subjected to t-PBC can be derived in a similar fashion. First, we re-write the potential energy  $V$  as a function of the scaled cylindrical coordinates and the components of matrix  $\mathbf{M}$ , as given in Eq. (8),

$$V(\{\mathbf{r}_i\}) = V(\{s_r^i, s_{\theta}^i, s_z^i\}, R, \phi, L_z) \quad (16)$$

The virial torque is then defined as the derivative of the free energy  $F$  with respect to  $\phi$ :

$$\tau \equiv \frac{\partial F}{\partial \phi} \quad (17)$$

$$F = -k_B T \ln \left\{ \frac{\Omega^N}{\Lambda^{3N} N!} \int d^{3N} \mathbf{s}_i \exp \left[ -\frac{V(\{s_r^i, s_{\theta}^i, s_z^i\}, R, \phi, L_z)}{k_B T} \right] \right\} \quad (18)$$

Since  $\partial\Omega/\partial\phi = 0$ , the torque reduces to

$$\tau = \frac{\int d^{3N} \mathbf{s}_i \exp \left[ -\frac{V(\{s_r^i, s_\theta^i, s_z^i\}, R, \phi, L_z)}{k_B T} \right] \frac{\partial V}{\partial \phi}}{\int d^{3N} \mathbf{s}_i \exp \left[ -\frac{V(\{s_r^i, s_\theta^i, s_z^i\}, R, \phi, L_z)}{k_B T} \right]} \equiv \left\langle \frac{\partial V}{\partial \phi} \right\rangle \quad (19)$$

In other words, the torque  $\tau$  is simply the ensemble average of the derivative of the potential energy with respect to torsion angle  $\phi$ . To facilitate calculation in an atomistic simulation, we can express  $\partial V/\partial\phi$  in terms of the real coordinates of the atoms:

$$\frac{\partial V}{\partial \phi} = \frac{1}{L_z} \sum_{i=1}^{N-1} \sum_{j=i+1}^N -\frac{\partial V}{\partial(x_i - x_j)} (y_i z_i - y_j z_j) + \frac{\partial V}{\partial(y_i - y_j)} (x_i z_i - x_j z_j) \quad (20)$$

Hence we arrive at the virial torque expression

$$\tau = \frac{1}{L_z} \left\langle \sum_{i=1}^{N-1} \sum_{j=i+1}^N -\frac{\partial V}{\partial(x_i - x_j)} (y_i z_i - y_j z_j) + \frac{\partial V}{\partial(y_i - y_j)} (x_i z_i - x_j z_j) \right\rangle \quad (21)$$

There is no velocity term in Eq. (21) because modifying  $\phi$  does not change the volume  $\Omega$  of the wire. This expression is verified numerically in Appendix C in the zero temperature limit when the free energy equals to the potential energy. The corresponding quantity in continuum elasticity theory can be written in terms of an integral over the volume  $\Omega$  of the simulation cell:

$$\tau = Q_{zz} \equiv \frac{1}{L_z} \int_{\Omega} -y \sigma_{xz} + x \sigma_{yz} dV \quad (22)$$

The derivation is given in Appendix A. The stress in the above expression refers to the Cauchy stress in the context of finite deformation. Because it uses current coordinates, the expression remains valid in finite deformation. The correspondence between Eqs. (21) and (22) bears a strong resemblance to the correspondence between Eqs. (10) and (15). While the virial stress formula corresponds to the average (i.e. zeroth moment) of the stress field over volume  $\Omega$ ,  $\tau$  corresponds to a linear combination of the first moments of the stress field.

### 3.3. Virial bending moment in b-PBC

Following a similar procedure, we can obtain the virial expression for the bending moment for a simulation cell subjected to b-PBC. First, we rewrite the potential energy of a system under b-PBC as

$$V(\{\mathbf{r}_i\}) = V(\{s_r^i, s_\theta^i, s_z^i\}, R, \Theta, L_z) \quad (23)$$

The virial bending moment is then the derivative of the free energy with respect to  $\Theta$ :

$$M \equiv \frac{\partial F}{\partial \Theta} \quad (24)$$

$$F = -k_B T \ln \left\{ \frac{\Omega^N}{A^{3N} N!} \int d^{3N} \mathbf{s}_i \exp \left[ -\frac{V(\{s_r^i, s_\theta^i, s_z^i\}, R, \Theta, L_z)}{k_B T} \right] \right\} \quad (25)$$

Again, we find that  $M$  is simply the ensemble average of the derivative of potential energy with respect to  $\Theta$ :

$$M = \left\langle \frac{\partial V}{\partial \Theta} \right\rangle \quad (26)$$

The derivative  $\partial V/\partial\Theta$  can be expressed in terms of the real coordinates of the atoms:

$$\frac{\partial V}{\partial \Theta} = \frac{1}{\Theta} \sum_{i=1}^{N-1} \sum_{j=i+1}^N -\frac{\partial V}{\partial(x_i - x_j)} (y_i \theta_i - y_j \theta_j + \rho \cos \theta_i - \rho \cos \theta_j) + \frac{\partial V}{\partial(y_i - y_j)} (x_i \theta_i - x_j \theta_j - \rho \sin \theta_i + \rho \sin \theta_j) \quad (27)$$

Hence we arrive at the virial bending moment expression:

$$M = \frac{1}{\Theta} \left\langle \sum_{i=1}^{N-1} \sum_{j=i+1}^N -\frac{\partial V}{\partial(x_i - x_j)} (y_i \theta_i - y_j \theta_j + \rho \cos \theta_i - \rho \cos \theta_j) + \frac{\partial V}{\partial(y_i - y_j)} (x_i \theta_i - x_j \theta_j - \rho \sin \theta_i + \rho \sin \theta_j) \right\rangle \quad (28)$$

There is no velocity term in Eq. (28) because modifying  $\Theta$  does not change the volume  $\Omega$  of the wire. This expression is verified numerically in Appendix D in the zero temperature limit when the free energy equals to the potential energy. The corresponding quantity in continuum elasticity theory can be written in terms of an integral over the volume  $\Omega$

of the simulation cell:

$$\begin{aligned} M = Q_{z\theta} &= \frac{1}{\Theta} \int_A dA \int_0^\Theta d\theta (-y\sigma_{x\theta} + x\sigma_{y\theta}) \\ &= \frac{1}{\Theta} \int_A dA \int_0^\Theta d\theta r\sigma_{\theta\theta} = \frac{1}{\Theta} \int_\Omega \sigma_{\theta\theta} dV \end{aligned} \quad (29)$$

where  $A$  is the cross-section area of the continuum body subjected to b-PBC. The correspondence between Eqs. (28) and (30) bears a strong resemblance to the correspondence between Eqs. (10) and (15). Similar to  $\tau$ ,  $M$  also corresponds to a linear combination of the first moments of the stress field over the simulation cell volume.

#### 4. Numerical results

In this section, we demonstrate the usefulness of t-PBC and b-PBC described above by torsion and bending molecular dynamics simulations of Si NWs to failure. The interactions between Si atoms are described by the modified-embedded-atom-method (MEAM) potential (Baskes, 1992), which has been found to be more reliable in the study of the failure Si NWs than several other potential models for Si (Kang and Cai, 2007). We considered two NWs both oriented along the [111] direction with diameters  $D = 7.5$  and 10 nm and the same aspect ratio  $L_z/D = 2.27$ . To make sure the NW surface is well reconstructed, the NWs are annealed by MD simulations at 1000 K for 1 ps followed by a conjugate gradient relaxation. To save space, we only present simulation results on initially perfect NWs under torsion and bending deformation at  $T = 300$  K. The effects of temperature and initial surface defects on the failure behavior of Si NWs will be presented in a subsequent paper.

##### 4.1. Si NW under torsion

Simulations of Si NWs under torsion can be carried out easily using t-PBC. Before applying a torsion, we first equilibrate the NWs at the specified temperature and zero stress (i.e. zero axial force) by MD simulations under PBC where the NW length is allowed to elongate to accommodate the thermal strain. Fig. 3(a) and (c) shows the annealed Si NW structures. Subsequently, torsion is applied to the NW through t-PBC, where the twist angle  $\phi$  (between two ends of the NW) increases in steps of 0.02 rad ( $\approx 1.15^\circ$ ). For each twist angle, MD simulation under t-PBC is performed for 2 ps. The Nose–Hoover thermostat is used to maintain the temperature at  $T = 300$  K using the Stömer–Verlet time integrator (Bond et al., 1999) with a time step of 1 fs. The linear momentum  $P_z$  and angular momentum  $J_z$  are conserved within  $2 \times 10^{-10}$  eV ps  $A^{-1}$  and  $9 \times 10^{-7}$  eV ps, during the simulation, respectively. The twist angle continues to increase until the NW fails. If the virial torque at the end of the 2 ps simulation is lower than that at the beginning of the simulation, the MD simulation is continued in 2 ps increments without increasing the twist angle, until the bending moment increases. The purpose of this approach is to give enough simulation time to resolve the failure process whenever that occurs. The virial torque is computed by time averaging over the last 1 ps of the simulation for each twist angle. The torque versus twist angle relationship is plotted in Fig. 4.

The  $\tau$ - $\phi$  curve is linear for small values of  $\phi$  and becomes non-linear as  $\phi$  approaches the critical value at failure. The torsional stiffness can be obtained from the torque–twist relationship and its value at small  $\phi$  can be compared to theory. The torsional stiffness is defined as

$$k_t \equiv \frac{\partial \tau}{\partial \phi} \quad (30)$$

In the limit of  $\phi \rightarrow 0$ , the torsional stiffness is estimated to be  $k_t = 5.11 \times 10^3$  eV for  $D = 7.5$  nm and  $k_t = 1.25 \times 10^4$  eV for  $D = 10$  nm. Strength of materials predicts the following relationships for elastically isotropic circular shafts under torsion:

$$\tau = \frac{\phi}{L_z} GJ, \quad k_t = \frac{GJ}{L_z} \quad (31)$$

where  $G$  is the shear modulus,  $J = \pi D^4/32$  is the polar moment of inertia. We note that this expression is valid only in the limit of small deformation ( $\phi \rightarrow 0$ ). To compare our simulation results against this expression, we need to use the shear modulus of Si given by the MEAM model ( $C_{11} = 163.78$  GPa,  $C_{12} = 64.53$  GPa,  $C_{44} = 76.47$  GPa) on the (1 1 1) plane, which is  $G = 58.57$  GPa. The predictions of the torsional stiffness from strength of materials are compared with the estimated value from MD simulations in Table 1. The predictions overestimate the MD results by 25–30%. However, this difference can be easily eliminated by a slight adjustment ( $\sim 6\%$ ) of the NW diameter  $D$ , given that  $k_t \propto D^4$ . The adjusted diameters  $D^*$  for the two NWs is approximately 6 Å smaller than the nominal diameters  $D$ , which corresponds to a reduction of the NW radius by 3 Å. This can be easily accounted for by the inaccuracy in the definition of NW diameter and the possibility of a weak surface layer on Si NWs (Kang and Cai, 2007).

The above agreement gives us confidence in the use of strength of materials to describe the behavior of NWs under torsion. Hence, we will use it to extract the critical strain in both NWs at failure. The maximum strain (engineering strain)

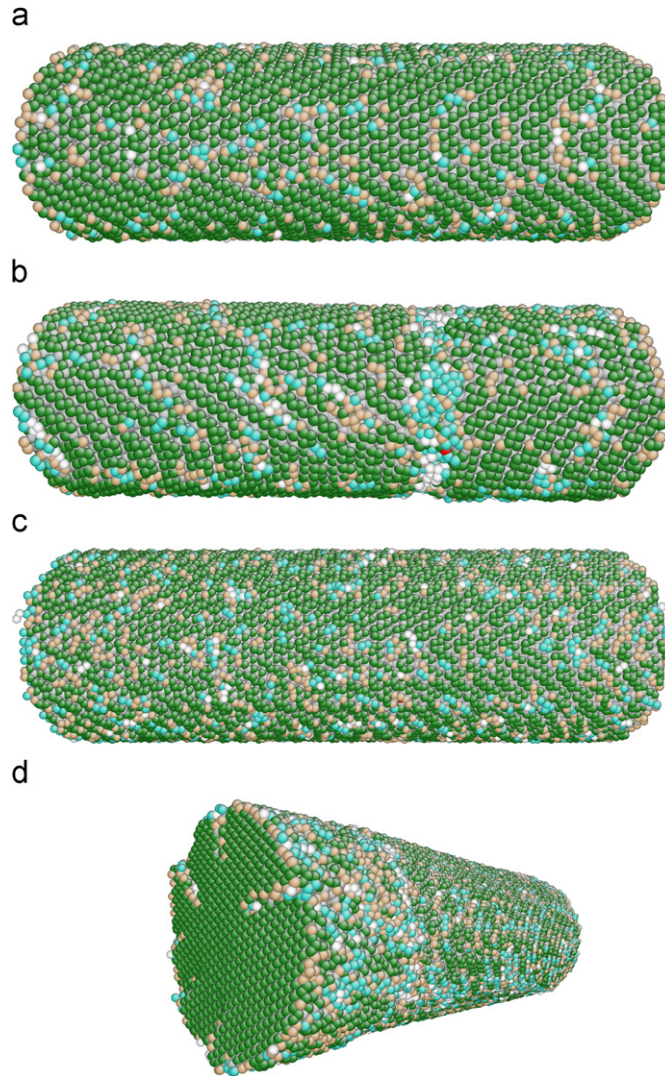


**Fig. 3.** Snapshots of Si NWs of two diameters before torsional deformation and after failure. The failure mechanism depends on its diameter. (a) Initial structure,  $D = 7.5$  nm. (b) After failure,  $D = 7.5$  nm,  $\phi = 1.16$  rad. (c) Initial structure,  $D = 10$  nm. (d) After failure,  $D = 10$  nm,  $\phi = 1.18$  rad.

in a cylindrical torsional shaft occurs on its surface:

$$\gamma_{\max} = \frac{\phi D}{2L_z} \quad (32)$$

Given that the aspect ratio of NWs is kept at  $L_z/D = 2.27$ , we have

$$\gamma_{\max} = 0.22\phi \quad (33)$$

for both NWs. The critical twist angle and critical strain at failure for both NWs are listed in Table 1.

We expect the critical shear strain at failure to be independent of the shaft diameter for large diameters. This seems to hold remarkably well in our NW torsion simulation. Because the NW under t-PBC has no “ends”, failure can initiate anywhere along the NW. However, different failure mechanisms are observed in the two NWs with different diameters. The thinner NW fails by sliding along a (1 1 1) plane, as seen in Fig. 3(b). The thicker NW fails by sliding both along a (1 1 1) plane and along longitudinal planes, creating wedges on the (1 1 1) cross-section, as seen in Fig. 3(d). The failure mechanism of the thicker NW is also more gradual than that of the thinner NW. As can be observed in Fig. 4, the torque is completely relieved on the thinner NW when failure occurs, whereas the thicker NW experiences a sequence of failures. A more detailed analysis on the size dependence of NW failure modes and their mechanisms will be presented in a subsequent paper.

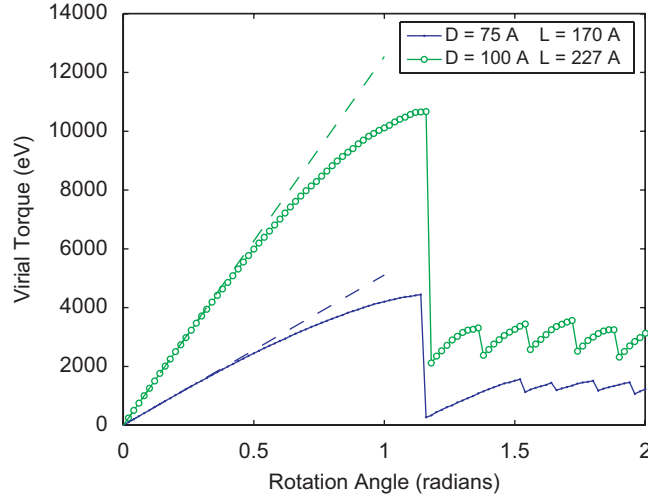


**Fig. 4.** Virial torque  $\tau$  as a function of rotation angle  $\phi$  between the two ends of the NWs of two different diameters. Because the two NWs have the same aspect ratio  $L_z/D$ , they have the same maximum strain (on the surface)  $\gamma_{\max} = \phi D/2L_z$  at the same twist angle  $\phi$ .

**Table 1**

Comparison of torsional stiffness for Si NW estimated from MD simulations and that predicted by strength of materials (SOM) theory

Nominal diameter, $D$ (nm)	$k_t$ (MD) (eV)	$k_t$ (SOM) (eV)	Adjusted diameter, $D^*$ (nm)	$\phi_c$	$\gamma_c$ (rad)
7.5	5110	6680	7.0	1.16	0.26
10.0	12538	15812	9.4	1.18	0.26

$D^*$  is the adjusted NW diameter that makes the SOM predictions exactly match MD results. The critical twist angle  $\phi_c$  and critical shear strain  $\gamma_c$  at failure are also listed.

#### 4.2. Si NW under bending

Simulations of Si NWs can be carried out using b-PBC just as we did for torsion. The Si NWs are equilibrated in the same way as described in the previous section before we apply bending through b-PBC. The bending angle  $\theta$  (between two ends of the NW) increases in steps of 0.02 rad ( $\approx 1.15^\circ$ ). For each twist angle, MD simulations under b-PBC were performed for 2 ps. The linear momentum  $P_z$  and angular momentum  $J_z$  is conserved to the same level of precision as in the torsion simulations. The bending angle continues to increase until the NW fails. If the virial bending moment at the end of the 2 ps simulation is lower than that at the beginning of the simulation, the MD simulation is continued in 2 ps increments without increasing the bending angle, until the bending moment increases. The purpose of this approach is to give enough simulation time to resolve the failure process whenever that occurs. The virial bending moment is computed by a time average over the last 1 ps of the simulation for each twist angle. The bending moment versus bending angle relationship is plotted in Fig. 5.

The  $M-\theta$  curve is linear for small values of  $\theta$  and becomes non-linear as  $\theta$  approaches the critical value at failure. The bending stiffness can be computed from the  $M-\theta$  curve and its value at small  $\theta$  can be compared to theory. Similar to the torsional stiffness in the previous section, we define a bending stiffness as

$$k_b \equiv \frac{\partial M}{\partial \theta} \quad (34)$$

In the limit of  $\theta \rightarrow 0$  the bending stiffness is estimated to be  $k_b = 8.12 \times 10^3$  eV for  $D = 7.5$  nm and  $k_b = 1.96 \times 10^4$  eV for  $D = 10$  nm. Strength of materials predicts the following relationships for elastically isotropic beam under bending:

$$M = \frac{\theta}{L_0} E I_z, \quad k_b = \frac{E I_z}{L_0} \quad (35)$$

where  $E$  is Young's modulus,  $I_z = \pi D^4/64$  is the moment of inertia of the NW cross-section around  $z$ -axis. To compare our simulation results against this expression, we need to use Young's modulus of Si given by the MEAM model along the  $[111]$  direction, which is 181.90 GPa. The predictions of the torsional stiffness from strength of materials are compared with the estimated value from MD simulations in Table 2. The predictions overestimate the MD results by 23–25%. But this difference can be easily eliminated by a slight adjustment ( $\sim 5\%$ ) of the NW diameter  $D$ , given that  $k_b \propto D^4$ . The adjusted diameters  $D^*$  for the two NWs is approximately 5 Å smaller than the nominal diameters  $D$ , which corresponds to a

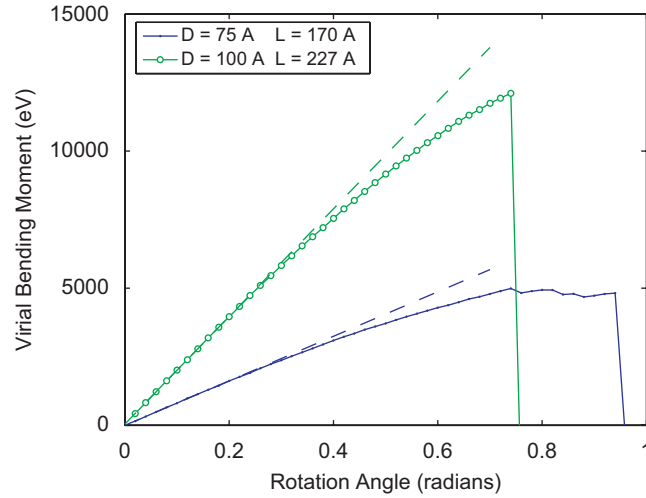


**Fig. 5.** Virial bending moment  $M$  as a function of bending angle  $\theta$  between the two ends of the two NWs with different diameters. Because the two NWs have the same aspect ratio  $L_z/D$ , they have the same maximum strain  $\varepsilon_{\max} = \theta D/2L_z$  at the same bending angle  $\theta$ .

**Table 2**

Comparison of the bending stiffnesses for Si NWs estimated from MD simulations and that predicted by strength of materials (SOM) theory

Nominal diameter, $D$ (nm)	$k_b$ (MD) (eV)	$k_b$ (SOM) (eV)	Adjusted diameter, $D^*$ (nm)	$\theta_f$ (rad)	$\varepsilon_f$
7.5	8117	10374	7.1	0.96	0.21
10.0	19619	24554	9.5	0.76	0.17

$D^*$  is the adjusted NW diameter that makes SOM predictions exactly match MD results. The critical bending angle  $\theta_f$  and critical normal strain  $\varepsilon_f$  at fracture are also listed.

reduction of the NW radius by 2.5 Å. It is encouraging to see that the adjusted diameters from torsion simulations match those for the bending simulations reasonably well.

The above agreement gives us confidence in the use of strength of materials theory to describe the behavior of NW under bending. Hence we will use it to extract the critical strain experienced by both NWs at the point of fracture. Based on the strength of materials theory, the maximum strain (engineering strain) of a beam in pure bending occurs at the points furthest away from the bending axis,

$$\varepsilon_{\max} = \frac{\theta D}{2L_0} \quad (36)$$

Since the aspect ratio of NWs is kept at  $L_0/D = 2.27$ , we have

$$\varepsilon_{\max} = 0.22\theta \quad (37)$$

for both NWs. The critical bending angle and critical normal strain at failure for both NWs are listed in Table 2. The critical strain at fracture is similar to results obtained from MD simulations of Si NWs under uniaxial tension,  $\varepsilon_f = 0.18$ , also using the MEAM model (Kang and Cai, 2007). The higher critical stress value observed in the thinner NW in bending is related to the higher stress gradient across its cross-section.

Fig. 6 shows the atomic structure of the NWs right before and right after fracture. The much larger critical strain observed in the thinner NW is related to the formation of metastable hillocks on the compressible side of the NW, as shown in Fig. 6(a). It seems that the formation of hillocks relieves some bending strain and allows the thinner NW to deform further without causing fracture. In fact, the onset of hillock formation in the thinner NW happens at the same rotation angle ( $\theta = 0.76$  rad) as the angle at which the thicker NW fractures. The detailed mechanisms responsible for the size and possible temperature dependence of NW failure modes in bending will be presented in a subsequent paper.

## 5. Summary

In this work we have presented a unified approach to handle torsion and bending of wires in atomistic simulations by generalizing the Born–von Kármán periodic boundary conditions to cylindrical coordinates. We provided

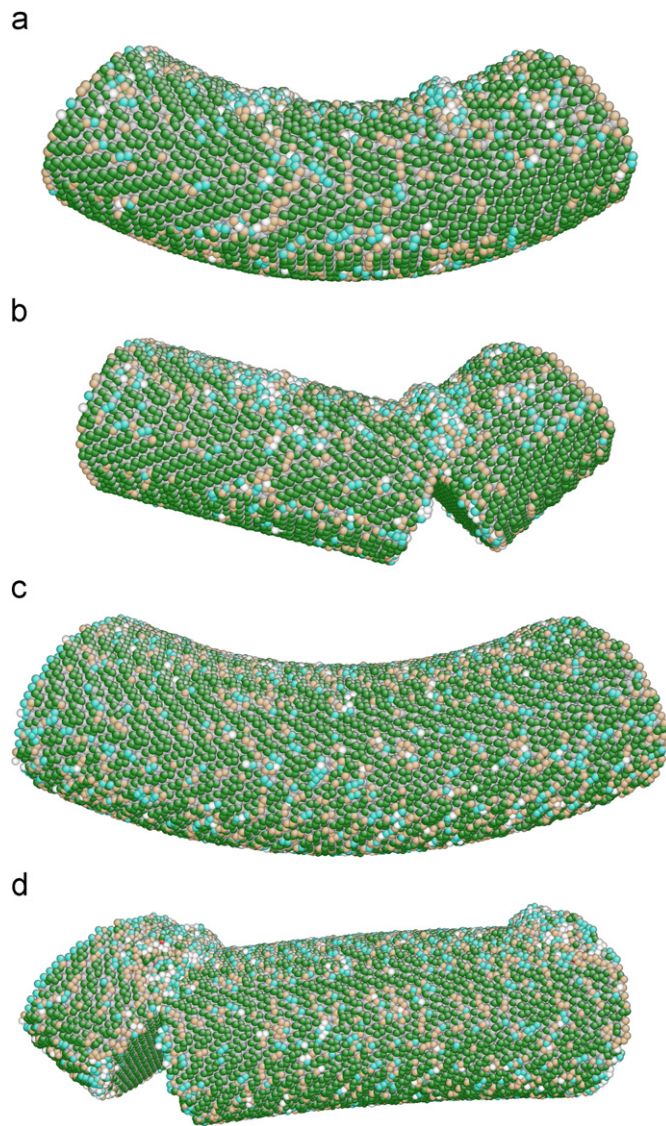


**Fig. 6.** Snapshots of Si NWs of two diameters under bending deformation before and after fracture. While metastable hillocks form on the thinner NWs before fracture (a), this does not happen for the thicker NW (c). (a) Before fracture,  $D = 7.5$  nm,  $\phi = 0.94$  rad. (b) After fracture,  $D = 7.5$  nm,  $\phi = 0.96$  rad. (c) Before fracture,  $D = 10$  nm,  $\phi = 0.74$  rad. (d) After fracture,  $D = 10$  nm,  $\phi = 0.76$  rad.

the expressions for the torque and bending moments in terms of an average over the entire simulation cell, in close analogy to the virial stress expression. Molecular dynamics simulations under these new boundary conditions show several failure modes of silicon nanowires under torsion and bending, depending on the nanowire diameter. These simulations are able to probe the intrinsic behavior of nanowires because the artificial end effects are completely removed.

### Acknowledgments

We would like to thank Prof. D.M. Barnett for helpful comments on this manuscript and Keonwook Kang for his kind help with the MEAM potential and MD++. This work is supported by an NSF/CMMI Nano-Bio-Materials program Grant CMS-0556032. C.R. Weinberger is supported by a Benchmark Stanford Graduate Fellowship. W. Fong is supported by a National Defense Science and Engineering Graduate Fellowship. E. Elsen is supported by the U.S. Department of Energy ASC program under contract number LLNL B341491 as part of the Advanced Simulating and Computing Program (ASC).

## Appendix A. Continuum analogue of virial torque expression

In this appendix, we show that the corresponding expression for the virial torque given in Eq. (21):

$$\tau = \frac{1}{L_z} \left\langle \sum_{i=1}^{N-1} \sum_{j=i+1}^N -\frac{\partial V}{\partial(x_i - x_j)} (y_i z_i - y_j z_j) + \frac{\partial V}{\partial(y_i - y_j)} (x_i z_i - x_j z_j) \right\rangle$$

is given by Eq. (22):

$$\tau = Q_{zz} \equiv \frac{1}{L_z} \int_{\Omega} -y \sigma_{xz} + x \sigma_{yz} dV$$

The reader is referred to the classical text of Eshelby (1956) for a discussion of a related problem. To begin, let us consider a continuum body aligned along the  $x_j$ -axis and subjected to t-PBC as defined in Section 2.2. The two end surfaces of the continuum are planes perpendicular to the  $x_j$ -axis: a plane  $S^{(a,j)}$  on which  $x_j = x_j^{(a)}$ , and another plane  $S^{(b,j)}$  on which  $x_j = x_j^{(b)}$ , where  $x_j^{(b)} = x_j^{(a)} + L$ , as shown in Fig. A1. The surface normal vectors for both  $S^{(a,j)}$  and  $S^{(b,j)}$  planes point to the positive  $x_j$ -axis. The remaining surface area of the continuum body,  $S_c$ , is traction-free.  $Q_{ij}$  is defined as the moment around the  $x_i$ -axis due to the traction forces acting on these surfaces, which has a surface normal along the  $x_j$ -axis. Obviously, the virial torque  $\tau$  here should correspond to  $Q_{zz}$  because both the wire and the torque are along the  $z$ -axis. Hence our task is to show that  $Q_{zz}$  can be written into the form of Eq. (22).

We now derive the general expression for  $Q_{ij}$ . By definition, we can write  $Q_{ij}$  as a surface integral:

$$\begin{aligned} Q_{ij} &\equiv \int_{S^{(a,j)}} (\mathbf{x} \times \mathbf{t})_i dS \\ &= \int_{S^{(a,j)}} \varepsilon_{ikl} x_k \sigma_{ml} n_m dS \end{aligned} \quad (\text{A.1})$$

where  $\mathbf{n}$  is the normal vector of the surface,  $\sigma_{ml}$  is the stress field, and we have used the fact that  $F_l = \sigma_{ml} n_m$ . At equilibrium, the moment evaluated at  $S^{(a,j)}$  and  $S^{(b,j)}$  must equal each other, i.e.

$$Q_{ij} = \int_{S^{(a,j)}} \varepsilon_{ikl} x_k \sigma_{ml} n_m dS = \int_{S^{(b,j)}} \varepsilon_{ikl} x_k \sigma_{ml} n_m dS \quad (\text{A.2})$$

Let us now consider the piece of continuum that is enclosed by the two cross-sections,  $S^{(a,j)}$  and  $S^{(b,j)}$ . Let  $S$  be the surface area of this continuum that consists of three parts,  $-S^{(a,j)}$ ,  $S^{(b,j)}$  and  $S_c$ , as shown in Fig. A1. In other words, the local outward surface normal for  $S$  is parallel to the normal vector of  $S^{(b,j)}$  but is anti-parallel to the normal vector of  $S^{(a,j)}$ . We can show that  $Q_{ij}$  can be written as an integral over the entire surface  $S$ :

$$Q_{ij} = \frac{1}{x_j^{(b)} - x_j^{(a)}} \oint_S \varepsilon_{ikl} x_k x_j \sigma_{ml} n_m dS \quad (\text{A.3})$$

Notice that the extra term  $x_j$  in Eq. (A.3) takes two different constant values on the two surfaces  $S^{(b,j)}$  and  $S^{(a,j)}$ . To show that Eq. (A.3) is equivalent to Eq. (A.2), we used the fact that  $x_j = x_j^{(a)}$  on  $S^{(a,j)}$ ,  $x_j = x_j^{(b)}$  on  $S^{(b,j)}$  and  $S_c$  is traction-free. Therefore,

$$\begin{aligned} &\frac{1}{x_j^{(b)} - x_j^{(a)}} \oint_S \varepsilon_{ikl} x_k x_j \sigma_{ml} n_m dS \\ &= \frac{1}{x_j^{(b)} - x_j^{(a)}} \left[ x_j^{(b)} \int_{S^{(b,j)}} \varepsilon_{ikl} x_k \sigma_{ml} n_m dS - x_j^{(a)} \int_{S^{(a,j)}} \varepsilon_{ikl} x_k \sigma_{ml} n_m dS \right] \\ &= \int_{S^{(b,j)}} \varepsilon_{ikl} x_k \sigma_{ml} n_m dS \end{aligned} \quad (\text{A.4})$$

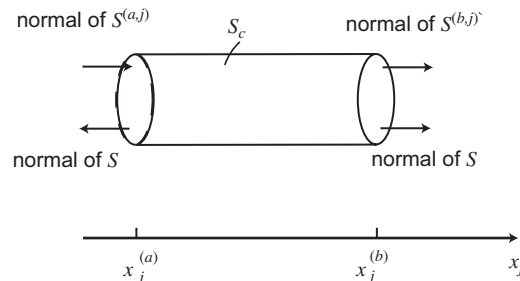


Fig. A1. A continuum body subjected to t-PBC whose surface  $S$  consists of three pieces:  $-S^{(a,j)}$ ,  $S^{(b,j)}$  and  $S_c$  (see text).

Now that Eq. (A.3) expresses  $Q_{ij}$  as an integral over a closed surface, we apply Gauss's Theorem and obtain

$$\begin{aligned} Q_{ij} &= \frac{1}{x_j^{(b)} - x_j^{(a)}} \int_{\Omega} (\varepsilon_{ikl} x_k x_j \sigma_{ml})_{,m} dV \\ &= \frac{1}{x_j^{(b)} - x_j^{(a)}} \int_{\Omega} \varepsilon_{ikl} (x_k x_j)_{,m} \sigma_{ml} + \varepsilon_{ikl} x_k x_j \sigma_{ml,m} dV \end{aligned} \tag{A.5}$$

Given  $x_{k,l} = \delta_{kl}$ , and the equilibrium condition  $\sigma_{ml,l} = 0$ , we have

$$\begin{aligned} Q_{ij} &= \frac{1}{x_j^{(b)} - x_j^{(a)}} \int_{\Omega} \varepsilon_{ikl} (\delta_{km} x_j + x_k \delta_{jm}) \sigma_{ml} dV \\ &= \frac{1}{x_j^{(b)} - x_j^{(a)}} \int_{\Omega} \varepsilon_{ikl} x_j \sigma_{kl} + \varepsilon_{ikl} x_k \sigma_{jl} dV \end{aligned} \tag{A.6}$$

Due to the symmetry of the stress tensor,  $\varepsilon_{ikl} \sigma_{kl} = 0$ . Hence

$$Q_{ij} = \frac{1}{x_j^{(b)} - x_j^{(a)}} \int_{\Omega} \varepsilon_{ikl} x_k \sigma_{jl} dV \tag{A.7}$$

In the special case of  $x_i = z$  and  $x_j = z$ , we have

$$T = Q_{zz} = \frac{1}{L_z} \int_{\Omega} x \sigma_{yz} - y \sigma_{xz} dV \tag{A.8}$$

We mention in passing that, for a straight rod aligned along the  $x$ -axis, the bending moment around the  $z$ -axis exerted at its ends can be expressed as

$$M = Q_{zx} = \frac{1}{L_x} \int_{\Omega} x \sigma_{yx} - y \sigma_{xx} dV \tag{A.9}$$

This expression is useful only when the rod is infinitely long and periodic along the  $x$ -axis. However, an initially straight rod subject to finite bending moment will become curved (and violates PBC), so that the above equation can no longer be used. In this case, we need to express the bending moment and the tensor  $Q$  in cylindrical coordinates (b-PBC) as in the next section.

### Appendix B. Continuum analogue of virial bending expression

In this appendix, we show that the corresponding expression for virial bending moment given in Eq. (28):

$$M = \frac{1}{\Theta} \left\langle \sum_{i=1}^{N-1} \sum_{j=i+1}^N -\frac{\partial V}{\partial (x_i - x_j)} (y_i \theta_i - y_j \theta_j + \rho \cos \theta_i - \rho \cos \theta_j) + \frac{\partial V}{\partial (y_i - y_j)} (x_i \theta_i - x_j \theta_j - \rho \sin \theta_i + \rho \sin \theta_j) \right\rangle$$

is given by Eq. (30):

$$\begin{aligned} M &= Q_{z\theta} = \frac{1}{\Theta} \int_A dA \int_0^{\Theta} d\theta (-y \sigma_{x\theta} + x \sigma_{y\theta}) \\ &= \frac{1}{\Theta} \int_A dA \int_0^{\Theta} d\theta r \sigma_{\theta\theta} = \frac{1}{\Theta} \int_{\Omega} \sigma_{\theta\theta} dV \end{aligned}$$

The constructions in the previous section can be generalized to bending by using cylindrical coordinates to show this.

Consider a continuum body aligned along the  $\theta$ -axis and subjected to b-PBC as defined in Section 2.3. The two end surfaces of the continuum are planes perpendicular to the  $\theta$ -axis: plane  $S^{(a,\theta)}$  on which  $\theta = \theta_a$ , and another plane  $S^{(b,\theta)}$  on which  $\theta = \theta_b$ , where  $\theta_b = \theta_a + \Theta$ , as shown in Fig. B1. The normal vectors of both planes are in the positive  $\theta$ -direction. The remaining surface area of the continuum body,  $S_c$ , is traction-free. To simplify some of the notations, the cross-section of

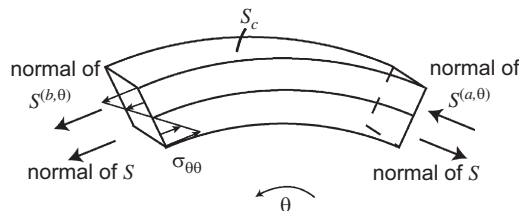


Fig. B1. A continuum body subjected to b-PBC whose surface  $S$  consists of three pieces:  $-S^{(a,\theta)}$ ,  $S^{(b,\theta)}$  and  $S_c$  (see text).

the continuum body is assumed to be rectangular. The main conclusion in this section remains valid for a circular cross-section.  $Q_{z\theta}$  is the bending moment (around  $z$ ) due to the traction on the half-plane  $S^{(a,\theta)}$  is

$$\begin{aligned} Q_{z\theta} &= \int_{S^{(a,\theta)}} (\mathbf{x} \times \mathbf{t})_z \, dS \\ &= \int_{S^{(a,\theta)}} (-y\sigma_{xk} + x\sigma_{yk})n_k \, dS \end{aligned} \quad (\text{B.1})$$

At equilibrium, the bending moment evaluated at half-plane  $S^{(a,\theta)}$  and  $S^{(b,\theta)}$  must be equal because the total moment on the continuum contained inside the wedge between the two half-planes should be zero. Therefore,

$$Q_{z\theta} = \int_{S^{(a,\theta)}} (-y\sigma_{xk} + x\sigma_{yk})n_k \, dS = \int_{S^{(b,\theta)}} (-y\sigma_{xk} + x\sigma_{yk})n_k \, dS \quad (\text{B.2})$$

Now consider the continuum contained between the two half-planes  $S^{(a,\theta)}$  and  $S^{(b,\theta)}$ . The total surface area of this continuum is  $S$ , which consists of  $-S^{(a,\theta)}$ ,  $S^{(b,\theta)}$  and  $S_c$  (traction free), as shown in Fig. B1. Similar to the previous section, we can show that

$$Q_{z\theta} = \frac{1}{\theta_b - \theta_a} \oint_S (-y\sigma_{xk} + x\sigma_{yk})\theta n_k \, dS \quad (\text{B.3})$$

Notice the extra term  $\theta$  in the integrand, which takes different values  $\theta$  on the two surfaces  $S^{(b,\theta)}$  and  $S^{(a,\theta)}$ . Applying Gauss's Theorem, we obtain

$$\begin{aligned} Q_{z\theta} &= \frac{1}{\Theta} \int_{\Omega} (-y\theta\sigma_{xk} + x\theta\sigma_{yk})_{,k} \, dV \\ &= \frac{1}{\Theta} \int_{\Omega} -(y\theta)_{,k}\sigma_{xk} + (x\theta)_{,k}\sigma_{yk} \, dV \\ &= \frac{1}{\Theta} \int_{\Omega} -y\theta_{,k}\sigma_{xk} + x\theta_{,k}\sigma_{yk} \, dV \end{aligned} \quad (\text{B.4})$$

Since  $\partial\theta/\partial x = -y/r^2$  and  $\partial\theta/\partial y = x/r^2$  we have

$$Q_{z\theta} = \frac{1}{\Theta} \int_{\Omega} (\sin^2\theta\sigma_{xx} + \cos^2\theta\sigma_{yy} - 2\sin\theta\cos\theta\sigma_{xy}) \, dV = \frac{1}{\Theta} \int_{\Omega} \sigma_{\theta\theta} \, dV \quad (\text{B.5})$$

Because the final expression, Eq. (B.5), may look counter-intuitive, in the following we will clarify its meaning using an alternative derivation. Indeed, since the wire is not subjected to a net tensile force, we expect the integral of  $\sigma_{\theta\theta}$  over any cross-section perpendicular to the  $\theta$ -axis to be zero. Hence one might expect the volume integral of  $\sigma_{\theta\theta}$  to be zero as well—but this is not the case.

Assume the cross-section area of the continuum body (beam) to be a rectangle with height  $h$  and width  $w$ , i.e.  $r \in [\rho - h/2, \rho + h/2]$  and  $z \in [-w/2, w/2]$ .  $r = \rho$  marks the neutral axis of the beam. Define  $\xi \equiv r - \rho$ . The bending moment on any cross-section perpendicular to the  $\theta$ -axis can be expressed as

$$M = \int_{-h/2}^{h/2} d\xi \int_{-w/2}^{w/2} dz \xi \sigma_{\theta\theta} \quad (\text{B.6})$$

Since the net tensile force on any cross-section should be zero, we have

$$\int_{-h/2}^{h/2} d\xi \int_{-w/2}^{w/2} dz \sigma_{\theta\theta} = 0 \quad (\text{B.7})$$

Hence we can re-write  $M$  as

$$\begin{aligned} M &= \int_{-h/2}^{h/2} d\xi \int_{-w/2}^{w/2} dz (\xi + \rho)\sigma_{\theta\theta} \\ &= \int_{\rho-h/2}^{\rho+h/2} dr \int_{-w/2}^{w/2} dz r\sigma_{\theta\theta} \end{aligned} \quad (\text{B.8})$$

At mechanical equilibrium, the value of  $M$  does not depend on the cross-section on which it is calculated. Hence we can also express  $M$  as an average over all possible cross-sections:

$$M = \frac{1}{\Theta} \int_{\rho-h/2}^{\rho+h/2} dr \int_{-w/2}^{w/2} dz \int_0^{\Theta} d\theta r\sigma_{\theta\theta} = \frac{1}{\Theta} \int_A dA \int_0^{\Theta} d\theta r\sigma_{\theta\theta} = \frac{1}{\Theta} \int_{\Omega} dV \sigma_{\theta\theta} \quad (\text{B.9})$$

### Appendix C. Numerical verification of the virial torque formula

In this appendix, we provide numerical verification for the virial torque expression, Eq. (21), in the limit of zero temperature. Because the free energy is the same as the potential energy at zero temperature, what this test really verifies is Eq. (20) for the derivative of potential energy with respect to twist angle  $\phi$ .

In this test case, we examine a small Si NW described by the Stillinger–Weber (SW) potential (Stillinger and Weber, 1985). This is different from the MEAM model we used in the MD simulations presented in Section 4. The reason to use the SW model here is its simplicity since we foresee that some readers may be interested in implementing t-PBC and b-PBC into their own simulation programs. While MD simulations under t-PBC and b-PBC require very little change to the existing programs, the calculation of the virial torque and bending moment requires modification to the subroutine that computes the virial stress, which is usually the same subroutine that computes the potential energy and forces on each atom. The modification is simple for simple models such as SW, Lennard-Jones (Allen and Tildesley, 2007), or embedded-atom-method (EAM) (Daw et al., 1993) potentials, but gets quite complicated for the MEAM model. The test case here provides a benchmark for potential readers who are interested enough to implement the virial torque expression in the SW model.

We did not use the SW model for MD simulations of Si NW in Section 4 for the following reasons. First, the elastic constants of SW model do not agree well with experimental values. The agreement is worse for the shear modulus than for Young's modulus. Because the elastic response of a wire under torsion is dictated by its shear modulus, the SW model predicts a very different torque–angle curve from what we would expect from an experiment (and from the predictions of MEAM potential). Second, the SW model (along with many other models) is known to predict an artificially ductile behavior for Si in MD simulations. In comparison, the MEAM model predicts the correct brittle behavior at low temperatures (Kang and Cai, 2007). Nonetheless, the SW model suffices to provide a simple test case to check the self-consistency of Eq. (20).

We prepared an NW along the  $[1\bar{1}0]$  orientation with diameter  $D = 3.2$  nm and length  $L_z = 13.8$  nm. The NW was annealed by MD simulation at 1000 K for 1 ps followed by conjugate gradient relaxation to a local energy minimum. After that, we applied a torsion by rotating the two ends of the NW with respect to each other in steps of  $\Delta\phi = 0.02$  rad. The atoms were relaxed to their minimum energy positions by conjugate gradient at each twist angle. Next, we took the relaxed configuration for  $\phi = 0.1$  and recorded the virial torque value as  $\tau_0 = 15.008629791$  eV. We then added an additional twist  $\pm\Delta\phi$  to it and computed the new potential energy  $V_{\pm}$  (without relaxation). The virial torque can be estimated from the numerical derivative of the potential energy:

$$\tau_{\text{num}} = \frac{V_+ - V_-}{2\Delta\phi} \quad (\text{C.1})$$

The values for  $\tau_{\text{num}}$  and the differences from  $\tau_0$  for different values of  $\Delta\phi$  are listed below.

$\Delta\phi$	$\tau_{\text{num}}$ (eV)	$\tau_{\text{num}} - \tau_0$ (eV)
$10^{-1}$	15.0081445307	$4.85 \times 10^{-4}$
$10^{-2}$	15.0086250291	$4.76 \times 10^{-6}$
$10^{-3}$	15.0086297599	$3.11 \times 10^{-8}$

(C.2)

The numerical differentiation converges to the virial torque formula at the speed of  $\mathcal{O}(\Delta\phi)^2$ , as it should. This confirms Eq. (20).

### Appendix D. Numerical verification of the virial bending moment formula

In this appendix, we provide numerical verification for the virial bending moment expression, Eq. (28), in the limit of zero temperature. Because the free energy is the same as the potential energy at zero temperature, what this test really verifies is Eq. (27) for the derivative of potential energy with respect to bending angle  $\theta$ . We also used the SW potential for Si here for simplicity.

The NW was created, equilibrated and relaxed in the same way as described in the previous section. After that we applied bending by rotating the two ends of the NW with respect to each other in steps of  $\Delta\theta = 0.02$  rad. The atoms were relaxed to their minimum energy positions by conjugate gradient at each value of  $\theta$ . We took the relaxed configuration for  $\theta = 0.1$  and recorded the virial bending moment as  $M_0 = 30.57105749653973$  eV. We then added an additional twist of  $\pm\Delta\theta$  to it and computed the new potential energy  $V_{\pm}$  (without relaxation). The virial bending moment can then be estimated from the numerical derivative of the potential energy:

$$M_{\text{num}} = \frac{V_+ - V_-}{2\Delta\theta} \quad (\text{D.1})$$

The values for  $M_{\text{num}}$  and the differences from  $M_0$  for different values of  $\Delta\theta$  are listed below:

$\Delta\theta$	$M_{\text{num}}$ (eV)	$M_{\text{num}} - M_0$ (eV)
$5 \times 10^{-2}$	30.566664661	$4.39 \times 10^{-3}$
$5 \times 10^{-3}$	30.571013585	$4.39 \times 10^{-5}$
$5 \times 10^{-4}$	30.571056959	$5.38 \times 10^{-7}$

(D.2)

The numerical differentiation converges to the virial bending moment expression at the speed of  $\mathcal{O}(\Delta\theta)^2$ , as it should. This confirms Eq. (28).

## References

- Allen, M.P., Tildesley, D.J., 2007. *Computer Simulation of Liquids*. Oxford University Press, Oxford.
- Baskes, M.I., 1992. Modified embedded-atom potentials for cubic materials and impurities. *Phys. Rev. B* 46, 2727–2742.
- Bond, S.D., Leimkuhler, B.J., Laird, B.B., 1999. The Nose–Poincaré method for constant temperature molecular dynamics. *J. Comput. Phys.* 151, 114–134.
- Bulatov, V.V., Cai, W., 2006. *Computer Simulations of Dislocations*. Oxford University Press, Oxford.
- Chau, M., Englander, O., Lin, L., 2003. Silicon nanowire-based nanoactuator. In: *Proceedings of the 3rd IEEE Conference on Nanotechnology*, vol. 2, San Francisco, CA, August 12–14, pp. 879–880.
- Chuang, K.S., Yip, S., 1991. Atomic-level stress in an inhomogeneous system. *J. Appl. Phys.* 70, 5688–5690.
- Cormier, J., Rickman, J.M., Delph, T.J., 2001. Stress calculation in atomistic simulations of perfect and imperfect solids. *J. Appl. Phys.* 89, 99–104.
- Cui, Y., Wei, Q., Park, H., Lieber, C.M., 2001. Nanowire nanosensors for highly sensitive and selective detection of biological and chemical species. *Science* 293, 1289–1292.
- Cui, Y., Zhong, Z., Wang, D., Wang, W.U., Lieber, C.M., 2003. High performance silicon nanowire field effect transistors. *Nano Lett.* 3, 149–152.
- Daw, M.S., Foiles, S.M., Baskes, M.I., 1993. The embedded-atom method: a review of theory and applications. *Mater. Sci. Eng. Rep.* 9, 251.
- Ding, W., Calabri, L., Chen, X., Kohlhass, K., Ruoff, R.S., 2006. Mechanics of crystalline boron nanowires. Presented at the 2006 MRS Spring Meeting, San Francisco, CA.
- Dumitrica, T., James, R.D., 2007. Objective molecular dynamics. *J. Mech. Phys. Solids* 55, 2206–2236.
- Eshelby, J.D., 1956. The continuum theory of lattice defects. *Solid State Phys.* 3, 79–144.
- Fan, R., Karnik, R., Yue, M., Li, D.Y., Majumdar, A., Yang, P.D., 2005. DNA translocation in inorganic nanotubes. *Nano Lett.* 5, 1633–1637.
- Horstemeyer, M.F., Lim, J., Lu, W.Y., Mosher, D.A., Baskes, M.I., Prantil, V.C., Plimpton, S.J., 2002. Torsion/simple shear of single crystal copper. *J. Eng. Mater. Technol.* 124, 322–328.
- Huang, Y., Lieber, C.M., 2004. Integrated nanoscale electronics and optoelectronics: exploring nanoscale science and technology through semiconductor nanowires. *Pure Appl. Chem.* 76, 2051–2068.
- Huhtala, M., Kuronen, A., Kaski, K., 2004. Dynamical simulations of carbon nanotube bending. *Int. J. Modern Phys. C* 15, 517–534.
- Isono, Y., Kiuchi, M., Matsui, S., 2006. Development of electrostatic actuated nano tensile testing device for mechanical and electrical characteristics of FB deposited carbon nanowire. Presented at the 2006 MRS Spring Meeting, San Francisco, CA.
- Jeff, P.M., Fleck, N.A., 1994. The failure of composite tubes due to combined compression and torsion. *J. Mater. Sci.* 29, 3080–3084.
- Kang, K., Cai, W., 2007. Brittle and ductile fracture of semiconductor nanowires—molecular dynamics simulations. *Philos. Mag.* 87, 2169–2189.
- Kizuka, T., Takatani, Y., Asaka, K., Yoshizaki, R., 2005. Measurements of the atomistic mechanics of single crystalline silicon wires of nanometer width. *Phys. Rev. B* 72, 035333-1–6.
- Makeev, M.A., Srivastava, D., 2006. Silicon carbide nanowires under external loads: an atomistic simulation study. *Phys. Rev. B* 74, 165303.
- Marc, G., McMillian, W.G., 1985. The virial theorem. *Adv. Chem. Phys.* 58, 209–361.
- Mylvaganam, K., Vodenitcharova, T., Zhang, L.C., 2006. The bending–kinking analysis of a single-walled carbon nanotube—a combined molecular dynamics and continuum mechanics technique. *J. Mater. Sci.* 41, 3341–3347.
- Nakatani, A., Kitagawa, H., 2004. Atomistic study of size effect in torsion tests of nanowire. In: XXI ICTAM, 15–21 August. URL ([http://fluid.ippt.gov.pl/ictam04/text/sessions/docs/MS3/11122/MS3\\_11122.pdf](http://fluid.ippt.gov.pl/ictam04/text/sessions/docs/MS3/11122/MS3_11122.pdf)).
- Nozaki, T., Doyama, M., Kogure, Y., 2002. Computer simulation of high-speed bending deformation in copper. *Radiat. Eff. Defects Solids* 157, 217–222.
- Parrinello, M., Rahman, A., 1981. Polymorphic transitions in single crystals: a new molecular dynamics method. *J. Appl. Phys.* 52, 7182–7190.
- Sommerfeld, A., 1964. *Partial Differential Equations in Physics, Lectures on Theoretical Physics*, vol. VI. Academic Press, New York.
- Stillinger, F.H., Weber, T.A., 1985. Computer simulation of local order in condensed phase of silicon. *Phys. Rev. B* 31, 5262–5271.
- Stölken, J.S., Evans, A.G., 1998. A microbend test method for measuring the plasticity length scale. *Acta Mater.* 46, 5100–5115.
- Tsai, D.H., 1979. Virial theorem and stress calculation in molecular-dynamics. *J. Chem. Phys.* 70, 1375–1382.
- Wang, D., Wang, Q., Javey, A., Tu, R., Dai, H., 2003. Germanium nanowire field-effect transistors with SiO<sub>2</sub> and high-κ HfO<sub>2</sub>. *Appl. Phys. Lett.* 83, 2432–2434.
- Zhang, C., Shen, H., 2006. Buckling and postbuckling analysis of single-walled carbon nanotubes in thermal environments via molecular dynamics simulation. *Carbon* 44, 2608–2616.
- Zhu, Y., Espinosa, H.D., 2005. An electromechanical material testing system for in situ electron microscopy and applications. *Proc. Natl. Acad. Sci.* 102, 14503–14508.
- Zimmerman, J.A., Webb III, E.B., Hoyt, J.J., Jones, R.E., Klein, P.A., Bammann, D.J., 2004. Calculation of stress in atomistic simulation. *Modelling Simulation Mater. Sci. Eng.* 12, S319–S332.